



Spectral evolution of the $s = \frac{1}{2}$ antiferromagnetic Heisenberg model: From one to two dimensionsCheng Gu ¹, Zhao-Long Gu,¹ Shun-Li Yu ^{1,2,*} and Jian-Xin Li^{1,2,†}¹National Laboratory of Solid State Microstructures and School of Physics, Nanjing University, Nanjing 210093, China²Collaborative Innovation Center of Advanced Microstructures, Nanjing University, Nanjing 210093, China

(Received 24 August 2023; accepted 30 November 2023; published 13 December 2023)

We employ spin-cluster perturbation theory to investigate the evolution of the spin excitation spectra of the mixed-dimensional antiferromagnetic $s = \frac{1}{2}$ Heisenberg models from the one-dimensional chain to the two-dimensional square and honeycomb lattices by varying the spin interactions J_{\perp} across the chains relative to J_{\parallel} along the chains. In addition to the well-defined magnon excitations, the spectra of the Néel phases for both lattices exhibit anomalous high-energy continua that evolve continuously from the continuum of one-dimensional chain through increasing J_{\perp} . Notably, the key features of the continua at the two-dimensional limit for $J_{\perp}/J_{\parallel} = 1$ are well consistent with experimental observations in real materials. Our results indicate that these high-energy continua in the Néel phases are a result of spinon deconfinement, which is further supported by a random-phase-approximation analysis based on the spinon Hubbard models.

DOI: [10.1103/PhysRevB.108.224418](https://doi.org/10.1103/PhysRevB.108.224418)

I. INTRODUCTION

In conventional magnets with long-range magnetic orders, low-energy magnetic excitations are described by spin-wave theory, in which the elementary excitations are magnons with integral spin $s = 1$. In contrast, in one-dimensional antiferromagnetic (AFM) spin- $\frac{1}{2}$ systems, such as the AFM Heisenberg chain, quantum fluctuations destroy the long-range orders and cause their elementary excitations to be $s = \frac{1}{2}$ quasiparticles called spinons [1]. Spinons are created in pairs by spin-flip excitations, such as in inelastic neutron scattering (INS) [2–6] or resonant inelastic x-ray scattering experiments [7–10], which results in the spin excitations exhibiting as two-spinon continua. For example, in the Heisenberg spin- $\frac{1}{2}$ chain with only nearest-neighbor (NN) AFM exchange interaction, a prototypical system that can be solved exactly based on the Bethe ansatz [11], the spin-excitation spectrum appears as a complete continuum [3,4,12,13]. The fractionalized spinon excitation is not only a feature of the one-dimensional AFM spin chains but also exists in the two-dimensional quantum spin liquids [14–19], so the two-spinon continua are key experimental signatures for identifying the quantum spin liquid states. On the other hand, based on the picture of spinons, a single magnon excitation in the magnetically ordered phases can also be considered the confinement of two spinons [20–37], which is analogous to the confinement of quarks in particle physics where quarks are bounded into baryons and mesons. Thus, the confinement and deconfinement of the spinons in quantum magnetic systems have attracted considerable interest in recent studies.

For the magnetically ordered phases, although the low-energy magnon spectra predicted by linear spin-wave (LSW) theory are well consistent with the experimental results, the

high-energy anomalous continua have been observed recently in INS experiments [21–23,38,39]. For example, an INS experiment on the square-lattice compound $\text{Cu}(\text{DCOO})_2 \cdot 4\text{D}_2\text{O}$ has revealed a high-energy continuum around the $(\pi, 0)$ point in the Brillouin zone (BZ) [23], and a recent experiment on the honeycomb-lattice compound YbCl_3 has shown a more remarkable continuum existing around the corners (K point) of the BZ together with a relatively weak dome-shaped broad continuum extending to the whole BZ [38]. Although the nature of these anomalous continua is still under debate, there has been intense discussion regarding the possibility of the coexistence of conventional magnon excitations and deconfined spinons [20–37].

The fact that both one- and two-dimensional spin systems exhibit continua in their spectra motivates us to investigate the connection between them. Two-dimensional systems can be viewed as those composed of coupled one-dimensional chains, so we can study the evolution of excitation spectra from one to two dimensions by changing the interchain couplings. This may reveal the deconfinement and confinement of spinons from one to two dimensions and provide insight into the possible mechanisms behind the continua in two-dimensional magnetically ordered systems. Authors of previous studies on coupled spin chains have suggested that even small interchain interactions can stabilize long-range orders [40–45]. When magnetic orders start to develop, the confinement of the spinons will occur [5,46]. When the interchain interaction is small, we can use a mean-field approximation to decouple the interchain interactions and map the original system to separate chains with additional on-site magnetic fields, which can result in the confinement of spinons in the spin chains [42,47]. Moreover, experimental realizations of quasi-one-dimensional spin systems provide ideal platforms to study the physics in weakly coupled chains. Theoretical predictions that small interchain interactions can induce the confinement of the spinons have been supported by INS experiments on such materials [5,5,6,33,48–51]. For

*slyu@nju.edu.cn

†jxli@nju.edu.cn

instance, an INS experiment on $\text{ScCo}_2\text{V}_2\text{O}_8$ [5], which is believed to be a realization of the quasi-one-dimensional spin- $\frac{1}{2}$ XXZ model, has revealed long-range magnetic order, loss of spectral weight of the two-spinon continuum, and clear magnon dispersion at low temperatures. However, at high temperatures, it exhibits one-dimensional features with a complete two-spinon continuum. Thus, exploring the evolution of spin-excitation spectra with interchain couplings is also essential for understanding the spin dynamics of some quasi-one-dimensional systems with nonnegligible interchain exchange interactions.

In this paper, we utilize spin-cluster perturbation theory (CPT) to study the evolution of spin excitation spectra from a one-dimensional AFM chain to two-dimensional AFM square and honeycomb lattices by increasing the interchain coupling J_\perp from 0 to $J_\perp/J_\parallel = 1$, where J_\parallel is the exchange interaction along the chains. Our results show that a small interchain coupling can induce long-range AFM order, which is consistent with experimental observations in many quasi-one-dimensional materials exhibiting AFM ordered ground states at low temperatures [5,33,48–51]. The CPT results reveal that the continua, originating from spinon deconfinement in the one-dimensional chain, continuously evolve as the system transforms from the chain to two-dimensional lattices. Notably, even in the AFM Néel state at the two-dimensional limit ($J_\perp/J_\parallel = 1$), there remains a distinct high-energy continuum in the spin excitation spectrum. Specifically, for the square lattice, the continuum is mainly concentrated at the $(\pi, 0)$ point, while for the honeycomb lattice, the continuum is distributed over a large area around the Γ' point and forms a dome shape with its maximal intensity at the K point. Additionally, the magnon dispersions exhibit a local minimum at the $(\pi, 0)$ point of the square lattice and the K point of the honeycomb lattice, which obviously deviates from the results of LSW theory. The key features of the high-energy continua and magnon dispersions at $J_\perp/J_\parallel = 1$ agree well with the results of INS experiments on square- and honeycomb-lattice AFM materials [21–23,38]. The continuous evolution of the continua from one to two dimensions suggests that the continua in two dimensions in certain momentum regions at high energies are a result of partial deconfinement of the spinons, and the local minima in the magnon dispersions arise from the coupling between magnons and spinons. To further verify this viewpoint, we use the random-phase-approximation (RPA) method to study the spinon Hubbard models, which has been proven successful in studying the spin dynamics of Heisenberg models [31,34,52,53]. Within the RPA calculations, the continua arise from the particle-hole excitations corresponding to the two-spinon excitations. The RPA results successfully reproduce all the key features of the continua and magnon dispersions in the CPT results, thus providing strong support for the continua at high energies of the AFM Néel phases originating from the mechanism of partial spinon deconfinement.

II. MODEL AND METHOD

The mixed-dimensional AFM Heisenberg model composed of coupled spin chains we consider here is

given by

$$H = J_\parallel \sum_{\langle ij \rangle_\parallel} S_i \cdot S_j + J_\perp \sum_{\langle ij \rangle_\perp} S_i \cdot S_j, \quad (1)$$

where J_\parallel (J_\perp) denotes the NN exchange interaction along (across) the one-dimensional chains, and $\langle ij \rangle_\parallel$ ($\langle ij \rangle_\perp$) represents the corresponding bonds.

To obtain the reliable spin dynamical structure factor of the model in Eq. (1), we employ the CPT method for the spin systems [26,37]. The CPT method combines the exact diagonalization (ED) of a small cluster to capture short-range correlations and a perturbative treatment of intercluster couplings to obtain properties of the infinite lattice. The key advantage of the CPT method lies in its ability to approximate the excitation spectrum in the thermodynamic limit, thereby overcoming the limitation of the ED method, which is confined to handling small-sized systems, while the CPT method does not exactly consider the strongly correlated effects beyond the small clusters. Initially, the CPT method was used to study the single-particle excitation spectrum of the strongly correlated electron systems [54–58]. To extend the CPT method to the spin system, we map the spin- $\frac{1}{2}$ operators to the hard-core bosonic operators [59]:

$$S_i^+ = b_i^\dagger, \quad S_i^- = b_i, \quad S_i^z = b_i^\dagger b_i - \frac{1}{2}, \quad (2)$$

where b_i^\dagger and b_i are the creation and annihilation operators of the hard-core boson. The hard-core bosonic operators obey the following commutation relations:

$$[b_i, b_j] = [b_i^\dagger, b_j^\dagger] = 0, \quad [b_i, b_j^\dagger] = \delta_{ij}(1 - 2b_i^\dagger b_i), \quad (3)$$

and the hard-core constraint: the eigenvalue of $n_i = b_i^\dagger b_i$ is 0 or 1. The spin Hamiltonian in Eq. (1) can be rewritten in the form of the hard-core bosonic operators as

$$\begin{aligned} H = & \frac{1}{2} J_\parallel \sum_{\langle ij \rangle_\parallel} (b_i^\dagger b_j + \text{H.c.}) \\ & + J_\parallel \sum_{\langle ij \rangle_\parallel} n_i n_j - 2J_\parallel \sum_i n_i \\ & + \frac{1}{2} J_\perp \sum_{\langle ij \rangle_\perp} (b_i^\dagger b_j + \text{H.c.}) \\ & + J_\perp \sum_{\langle ij \rangle_\perp} n_i n_j - 2J_\perp \sum_i n_i. \end{aligned} \quad (4)$$

Now we can use the bosonic version of the CPT method [60,61]. In the CPT method, the original lattice is divided into identical clusters, which form a superlattice. Consequently, we can rewrite the Hamiltonian as $H = H_c + V$, where H_c is the cluster Hamiltonian and V represents the coupling between different clusters. Afterward, the original-lattice Green's function in matrix form is given by

$$g(\vec{k}, \omega + i\eta) = G(\omega + i\eta)[1 - V(\vec{k})G(\omega + i\eta)]^{-1}, \quad (5)$$

where \vec{k} is the wave vector in the BZ of the superlattice and ω is the frequency. Here, η is a broadening parameter, $G(\omega + i\eta)$ is the cluster Green's function and can be calculated by the ED at zero temperature [62], and $V(\vec{k})$ can be written as $V(\vec{k})_{\mu\nu} = \sum_R V_{\mu\nu}^{OR} e^{i\vec{k}\cdot R}$, where R is the superlattice index and μ, ν are

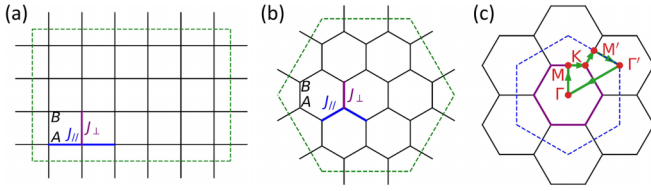


FIG. 1. (a) and (b) are clusters used in cluster perturbation theory (CPT) calculations for $J_{\perp}/J_{\parallel} \geq 0.5$ to tile the square and honeycomb lattices, respectively. (c) Path consisting of the high-symmetry points in the Brillouin zone (BZ) used to illustrate the excitation spectra for the honeycomb lattice.

the site indices in a cluster. Since in the CPT method the intercluster coupling in V should be quadratic, we perform the following mean-field approximation on the NN interactions [26,37]:

$$n_i n_j \rightarrow \langle n_i \rangle n_j + n_i \langle n_j \rangle. \quad (6)$$

Due to the fact that the original-lattice translation symmetry is broken in the CPT method, we carry out a periodization procedure and the Green's function is given by

$$g_{\text{cpt}}(k, \omega + i\eta) = \frac{1}{L} \sum_{\mu\nu} \exp[-ik \cdot (r_{\mu} - r_{\nu})] g_{\mu\nu}(\tilde{k}, \omega + i\eta), \quad (7)$$

where L is the number of sites in a cluster. Here, k denotes the wave vector in the BZ of the original lattice, and it can be expressed as $k = \tilde{k} + K$, where K is the reciprocal vector of the superlattice. The spin-dynamical structure factor $S^{+-}(k, \omega)$ is then given by

$$S^{+-}(k, \omega) = -\frac{1}{\pi} \text{Im} g_{\text{cpt}}(k, \omega + i\eta), \quad (8)$$

where $\eta = 0.15J_{\parallel}$ is used to determine the broadening of the spectrum.

As the CPT method does not exactly consider the strongly correlated effects beyond the small clusters, the obtained results still exhibit finite-sized effects [63]. In the following calculations for the square and honeycomb lattices, we employ two types of clusters. For the regime of weak interchain coupling where $J_{\perp}/J_{\parallel} < 0.5$, we use a 2×12 cluster. For $J_{\perp}/J_{\parallel} \geq 0.5$, we use the clusters as shown in Figs. 1(a) and 1(b), which maintain the point group symmetry of the original lattices as much as possible. All the calculations are carried out at zero temperature.

III. RESULTS

A. CPT results

Let us first discuss the case of the square lattice. For $J_{\perp} = 0$, the model becomes a set of completely decoupled spin chains, which has been well investigated by analytical and numerical methods [1,11,12,64]. In this case, the ground state is magnetically disordered due to the strong quantum fluctuations, and the elementary excitations are fractionalized $s = \frac{1}{2}$ spinons, which correspondingly results in a continuum of spin-excitation spectra. As shown in Fig. 2(a), the CPT method successfully reproduces the broad two-spinon

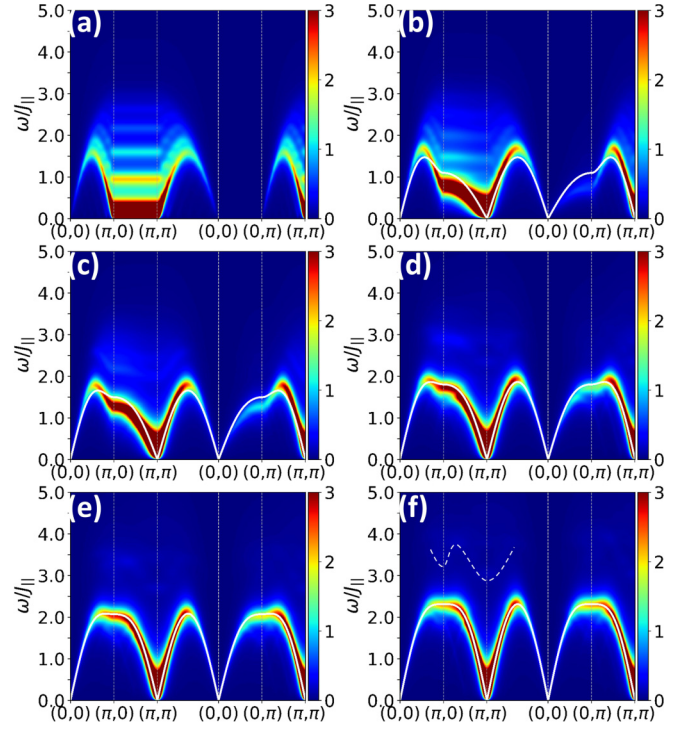


FIG. 2. Dynamical structure factor $S^{+-}(q, \omega)$ for the square-lattice Heisenberg model. (a)–(f) correspond to J_{\perp}/J_{\parallel} values of 0, 0.2, 0.4, 0.6, 0.8, and 1, respectively. The white solid lines represent the linear spin-wave (LSW) dispersion with the $1/S$ correction. The white dashed line in (f) indicates the lower boundary of the continuum. The unit of the color bar is $1/J_{\parallel}$.

continuum for $J_{\perp} = 0$ that is consistent with previous theoretical studies [12,65–67] and experimental observations [4]. When the interchain interactions are turned on, the coupling between chains will lead to the confinement of spinons via the inducing of an attractive interaction between spinon pairs and results in a magnetically ordered state [5]. In our calculation, we find that the AFM Néel transition, characterized by a nonzero average value of S^z on each site, occurs at $J_{\perp}^c = 0.025J_{\parallel}$, which is consistent with the experimental results of many quasi-one-dimensional materials exhibiting magnetic order at low temperatures [5,5,6,33,48–51]. According to the Bethe ansatz solution [11], the ground state of the one-dimensional AFM Heisenberg model already possesses quasi-long-range order with a spin-spin correlation function that decreases very slowly, as $1/r$ up to logarithmic corrections, so a small interchain coupling J_{\perp} can induce true long-range order. When $J_{\perp} > J_{\perp}^c$, gaps develop along the momentum direction from $(\pi, 0)$ to (π, π) with the only exception at (π, π) [see Fig. 2(b)]. The openings of these gaps are attributed to the effect of the interchain couplings, which produces the dispersion of the spinons in the direction perpendicular to the chains, and it provides a necessary condition for the Goldstone mode of the magnetic ordered phase at the (π, π) point. In the same way, excitation spectra also appear along the $(0, 0)$ to $(0, \pi)$ direction. In Figs. 2(b)–2(f), we also plot the magnon dispersion as a solid white line, which is calculated by LSW theory with $1/S$ correction [68]. One can see that the excitation spectra along the $(\pi, 0)$

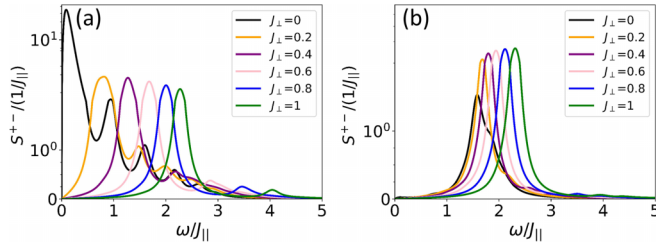


FIG. 3. Evolution of the energy distribution of $S^{+-}(q, \omega)$ for the square-lattice Heisenberg model with J_{\perp}/J_{\parallel} . (a) $q = (\pi, 0)$. (b) $q = (\pi/2, \pi/2)$.

to (π, π) and $(0, 0)$ to $(0, \pi)$ directions follow qualitatively the magnon dispersion, suggesting their magnon character. However, the energy of the magnons calculated by the CPT method is significantly lower than that predicted by LSW theory for a small J_{\perp} [see Figs. 2(b) and 2(c)]; this distinction is most notable in the vicinity of the $(\pi, 0)$ point. This indicates that the quantum fluctuations are strong for a small J_{\perp} and have the most significant impact on the spin excitation around the $(\pi, 0)$ point. Moreover, the continuum along $(\pi, 0)$ to (π, π) remain. With the further increase of the interchain coupling, the continuum becomes weaker, while the spectral intensity of the magnon becomes stronger and the magnon dispersion is more consistent with LSW theory with $1/S$ correction [Figs. 2(d)–2(f)], which is intimately related to the enhancement of AFM order. We notice that the spectrum exhibits a saddle point fixed at the $(\pi, 0)$ point, and the broad continuum evolves smoothly from one to two dimensions. As shown in Fig. 2(f), at the two-dimensional limit ($J_{\perp} = J_{\parallel}$), the saddle point at the $(\pi, 0)$ point becomes a local minimum in the magnon dispersion, whereas in contrast, the magnon dispersion in LSW theory is flat. Meanwhile, although the continuum becomes very weak overall at $J_{\perp} = J_{\parallel}$, it still retains significant intensities around the $(\pi, 0)$ point at high energies. These unconventional magnetic excitation characteristics in the AFM Néel phase obtained from the CPT calculations for $J_{\perp} = J_{\parallel}$, including the presence of a local minimum in the magnon dispersion at the $(\pi, 0)$ point and the existence of a high-energy continuum around the same point, are qualitatively consistent with the experimental observations in $\text{Cu}(\text{DCOO})_2 \cdot 4\text{D}_2\text{O}$ [23], a well-established example of the square-lattice NN Heisenberg AFM model with $J_{\perp} = J_{\parallel} = 6.11$ meV. The results for $J_{\perp} = J_{\parallel}$ are also consistent with the previous theoretical findings obtained from the variational Monte Carlo [23,25] and stochastic series expansion quantum Monte Carlo [24] approaches. To examine the weak continuum in two dimensions more closely, we present the evolutions of the spectra at $(\pi, 0)$ and $(\pi/2, \pi/2)$ points in Figs. 3(a) and 3(b), respectively. For $J_{\perp} = 0$, the line shape significantly deviates from the character of the single magnon excitation, namely, the Lorentz line shape. Instead, it consists of a complete two-spinon continuum, which is consistent with the exact results obtained using the Bethe ansatz [3,4,11,12]. As J_{\perp} increases, the spectra become closer to a standard Lorentz line shape, indicating that the elementary excitation changes from spinon to magnon. However, even for $J_{\perp} = J_{\parallel}$, a noticeable non-Lorentzian tail remains in the

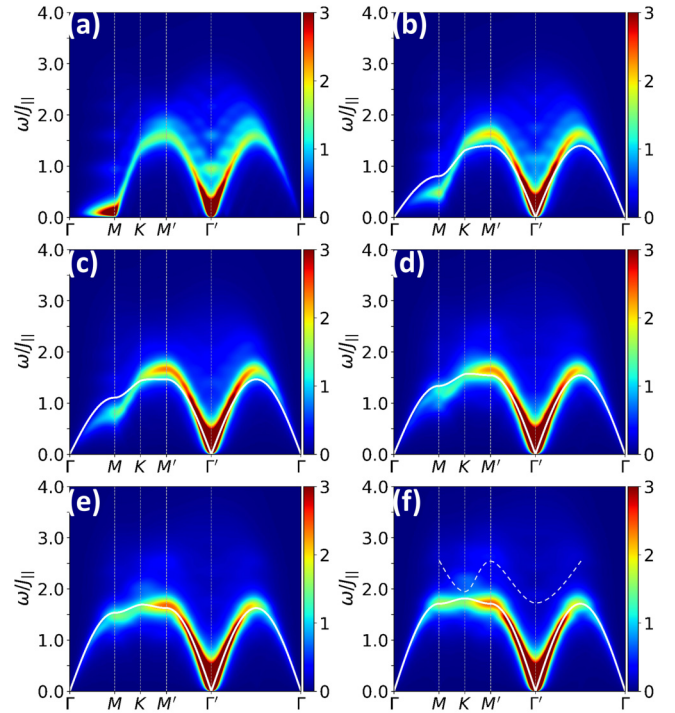


FIG. 4. Dynamical structure factor $S^{+-}(q, \omega)$ for the honeycomb-lattice Heisenberg model. (a)–(f) correspond to J_{\perp}/J_{\parallel} values of 0, 0.2, 0.4, 0.6, 0.8, and 1, respectively. The white solid lines represent the linear spin-wave (LSW) dispersion with the $1/S$ correction. The white dashed line in (f) indicates the lower boundary of the continuum. The unit of the color bar is $1/J_{\parallel}$.

spectrum at $(\pi, 0)$, which represents a residual two-spinon continuum. In contrast, at the $(\pi/2, \pi/2)$ point, the spectrum has already evolved into a Lorentzian line shape with a very small non-Lorentzian tail when J_{\perp}/J_{\parallel} is increased to 0.2. Thus, our results support that the high-energy continuum observed by INS in $\text{Cu}(\text{DCOO})_2 \cdot 4\text{D}_2\text{O}$ [23] originates from the deconfinement of spinons due to quantum fluctuations.

As is widely recognized, the honeycomb lattice exhibits stronger quantum fluctuations than the square lattice, owing to its lower coordination number. This is reflected in the fact that the system only displays AFM order when J_{\perp}/J_{\parallel} reaches 0.04 in our calculation, a threshold clearly higher than that for the square lattice. The evolution of the excitation spectra with interchain coupling J_{\perp}/J_{\parallel} is illustrated in Fig. 4. It is evident that the magnon dispersion calculated using the CPT method exhibits clearly significant deviations from the predictions of LSW theory shown as the white solid line in the figure, particularly near the K and M (M') points, which is a clear indication of the strong quantum fluctuations present on the honeycomb lattice. Although, like the square lattice, the continuum weakens as J_{\perp}/J_{\parallel} increases and the low-energy one-magnon excitations can be described by LSW theory with $1/S$ correction, there remains a more evident vestigial continuum than the square lattice even at the two-dimensional limit with $J_{\perp}/J_{\parallel} = 1$. A dome-shaped continuum with the upper boundary centering the Γ' point can be seen clearly and is consistent with the experimental observations in YbCl_3 [38]. We find that this dome-shaped continuum evolves con-

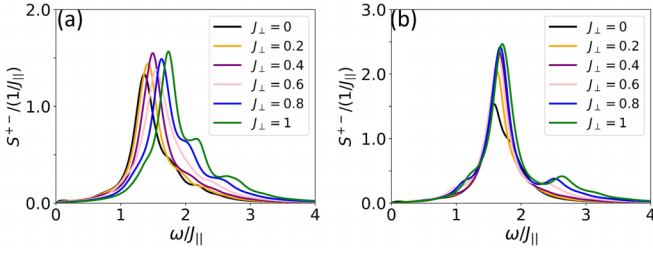


FIG. 5. Evolution of the energy distribution of $S^{+-}(q, \omega)$ for the honeycomb-lattice Heisenberg model with J_{\perp}/J_{\parallel} . (a) at K point. (b) at M' point.

tinuously from the spinon continuum in the one-dimensional case. Furthermore, as shown in Fig. 4(f) for $J_{\perp}/J_{\parallel} = 1$, the intensity of the continuum near the K point is significantly higher than those at other points. To make it clearer, we present the evolution of the spectra at K and M' points in Figs. 5(a) and 5(b), respectively. At the M' point, as J_{\perp} increases, the spectra become closer to a standard Lorentz line shape corresponding to the one-magnon excitations, and the small non-Lorentzian tail shifts to higher energies. In contrast, at the K point, the non-Lorentzian tail does not show an obvious decrease as J_{\perp} increases, and the line shape of the spectrum at $J_{\perp}/J_{\parallel} = 1$ does not differ significantly from that in the one-dimensional limit with $J_{\perp}/J_{\parallel} = 0$. This indicates that the spin excitations around the K point have obvious spinon-deconfinement characteristics, and there is even no well-defined one-magnon excitation. In contrast to the square lattice (Fig. 3), we find that the spectra on the honeycomb lattice display more pronounced continua deviating from the magnon excitations (Fig. 5), reflecting the fact that the honeycomb lattice possesses stronger quantum fluctuations than the square lattice. Moreover, as shown in Fig. 4(f), our CPT results demonstrate that the K point is a local minimum of the one-magnon dispersion. This finding is consistent with the experimental observation in YbCl_3 [38], which can be effectively described by the NN AFM Heisenberg model with $J_{\perp} = J_{\parallel} = 0.421$ meV. In contrast, according to LSW theory, the one-magnon dispersion at the K point is expected to possess a local maximum, represented by the solid white line in Fig. 4(f). On the other hand, we notice that this local minimum moves from M to K as J_{\perp}/J_{\parallel} is increased from 0 to 1, while the local minimum of in LSW theory is always at the M point without moving.

B. Comparisons between CPT and RPA results

Our CPT results indicate a close connection between the deconfinement of spinons and the anomalous continua in the two-dimensional Heisenberg model on the square and honeycomb lattices, via a systematic study of the spectrum evolution from one to two dimensions. To further support this viewpoint, we use the RPA method to analyze the spin-excitation spectra in the spinon Hubbard models. Evidently, in these models, the confinement and deconfinement of spinons give rise to magnons and continua, respectively. By comparing the CPT and RPA results, we can gain a deeper understanding of the origin of the anomalous continua in the two-dimensional Heisenberg models.

The spinon Hubbard model we consider here is

$$H = H_0 + U \sum_i n_{i\uparrow} n_{i\downarrow}, \quad (9)$$

where H_0 is the free part of the spinon Hamiltonian. For the square lattice, the π -flux resonating-valence-bond (RVB) ansatz is employed [69]:

$$H_0 = \sum_{i \in A, \sigma} (t_{\parallel} f_{i\sigma}^{\dagger} f_{i \pm \hat{x}\sigma} + e^{i\pi/2} t_{\perp} f_{i\sigma}^{\dagger} f_{i \pm \hat{y}\sigma} + \text{H.c.}), \quad (10)$$

where the sum only applies to one sublattice and $f_{i\sigma}^{\dagger}$ ($f_{i\sigma}$) is the creation (annihilation) operator of the spinon with spin σ at site i . For the honeycomb lattice, the uniform RVB ansatz is used [30]:

$$H_0 = \sum_{\langle ij \rangle_{\parallel} \sigma} (t_{\parallel} f_{i\sigma}^{\dagger} f_{j\sigma} + \text{H.c.}) + \sum_{\langle ij \rangle_{\perp} \sigma} (t_{\perp} f_{i\sigma}^{\dagger} f_{j\sigma} + \text{H.c.}). \quad (11)$$

Here, t_{\parallel} and t_{\perp} are the NN hoppings on the intrachain and interchain bonds, respectively, while $\langle ij \rangle_{\parallel}$ and $\langle ij \rangle_{\perp}$ represent the corresponding bonds.

To investigate the spin excitation of the AFM Néel phase, we decoupled the Hubbard interaction with the AFM order parameter, resulting in the following mean-field Hamiltonian:

$$H_{\text{MF}} = \sum_{\langle ij \rangle \sigma} (t_{ij} f_{i\sigma}^{\dagger} f_{j\sigma} + \text{H.c.}) - U \sum_i m_i (n_{i\uparrow} - n_{i\downarrow}). \quad (12)$$

Here, $m_A = -m_B = m$ represents the AFM order parameter, where A and B denote the two sublattices. For the square lattice, the mean-field dispersion is given by

$$E_{\pm}(k) = \pm \epsilon_k = \pm \sqrt{4(t_{\parallel}^2 \cos^2 k_x + t_{\perp}^2 \cos^2 k_y) + U^2 m^2}, \quad (13)$$

while for the honeycomb lattice, the dispersion takes the form:

$$E_{\pm}(k) = \pm \epsilon_k = \pm \sqrt{|t_{\parallel} [\exp(ik \cdot \delta_1) + \exp(ik \cdot \delta_2)] + t_{\perp}|^2 + U^2 m^2}, \quad (14)$$

where $\delta_1 = (-\frac{\sqrt{3}}{2}, -\frac{3}{2})$ and $\delta_2 = (\frac{\sqrt{3}}{2}, -\frac{3}{2})$. Furthermore, the AFM order parameter satisfies the self-consistent constraint $\frac{1}{U} = \frac{1}{N} \sum_k \frac{1}{\epsilon_k}$, where N is the number of lattice sites.

The bare-spin susceptibility for the mean-field Hamiltonian is expressed as follows:

$$\chi_{\alpha\beta}^{0,+}(q, i\omega_n) = \frac{1}{N_c} \int_0^{\beta} \exp(i\omega_n \tau) \langle T_{\tau} [S_{\alpha,q}^+(\tau) S_{\beta,-q}^-(0)] \rangle_0, \quad (15)$$

where $\alpha, \beta = A, B$ are the sublattice labels, N_c is the number of the unit cells, and $S_{\alpha,q}^{+/-} = \sum_R \exp[iq \cdot (R + r_{\alpha})] S_{\alpha,R}^{+/-}$, with R the unit cell index and r_{α} the position of the α sublattice in a unit cell. The RPA spin susceptibility is given by [52,53,70–72]

$$\chi^{+-} = \chi^{0,+} [1 - U \chi^{0,+}]^{-1}. \quad (16)$$

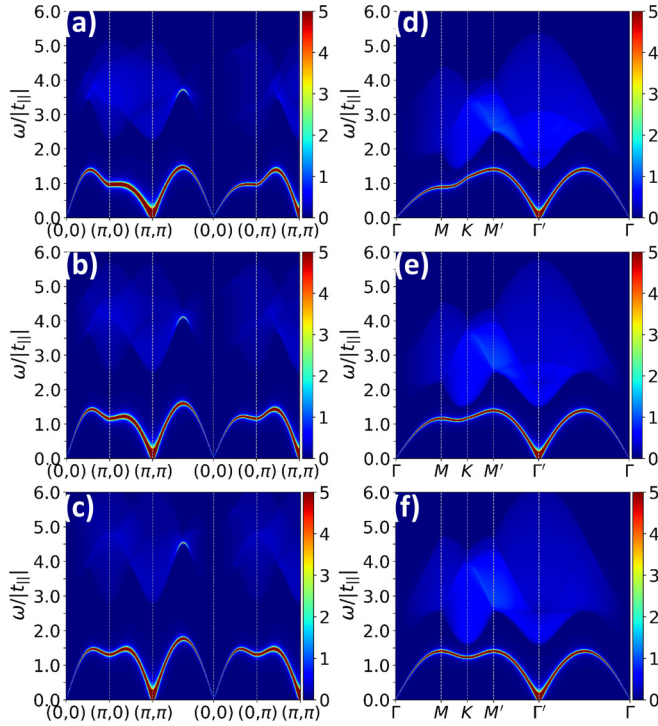


FIG. 6. Spectral functions obtained from the random-phase-approximation (RPA) calculations for the spinon Hubbard models on the square and honeycomb lattices. (a)–(c) for the square lattice with $t_{\perp}/t_{\parallel} = 0.6, 0.8,$ and 1 , respectively. (d)–(f) for the honeycomb lattice with $t_{\perp}/t_{\parallel} = 0.6, 0.8,$ and 1 , respectively. The unit of the color bar is $1/|t_{\parallel}|$.

Here, $\chi^{0,+}$ and χ^{+-} are matrices:

$$\chi^{0,+} = \begin{bmatrix} \chi_{AA}^{0,+} & \chi_{AB}^{0,+} \\ \chi_{BA}^{0,+} & \chi_{BB}^{0,+} \end{bmatrix}, \quad \chi^{+-} = \begin{bmatrix} \chi_{AA}^{+-} & \chi_{AB}^{+-} \\ \chi_{BA}^{+-} & \chi_{BB}^{+-} \end{bmatrix}. \quad (17)$$

Then we obtain the dynamical structure factor $S^{+-}(q, \omega) = \text{Im} \chi^{+-}(q, \omega + i\eta)/\pi$ with $\chi^{+-}(q, i\omega_n) = \sum_{ab} \chi_{ab}^{+-}(q, i\omega_n)$, and we focus on the spin dynamics at zero temperature. Our RPA analysis focuses on the AFM Néel phase, and we select three relatively large interchain hoppings with t_{\perp}/t_{\parallel} values of $0.6, 0.8,$ and 1.0 , for which the AFM order parameter remains relatively stable. Thus, we will fix the order parameter values, which will not qualitatively affect our subsequent analysis. For the square lattice, we set the mean-field AFM order parameter to $m = 0.3$. As shown in Figs. 6(a)–6(c) and 7, the RPA analysis based on the spinon Hubbard model reproduces all of the basic characteristics of the spin-excitation spectra obtained from the above CPT calculations based on the Heisenberg model. The magnon dispersion and its evolution with the interchain coupling in the RPA and CPT results are qualitatively consistent, especially that the saddle point is fixed at the $(\pi, 0)$ point and evolves into a local minimum at $t_{\perp}/t_{\parallel} = 1$ and $J_{\perp}/J_{\parallel} = 1$. In both CPT and RPA results, the continua above the magnon dispersions are predominantly concentrated in the regions around the $(\pi, 0)$ and (π, π) points, and the overall spectral weights of the continua are weakened with the increase of the interchain coupling. Like

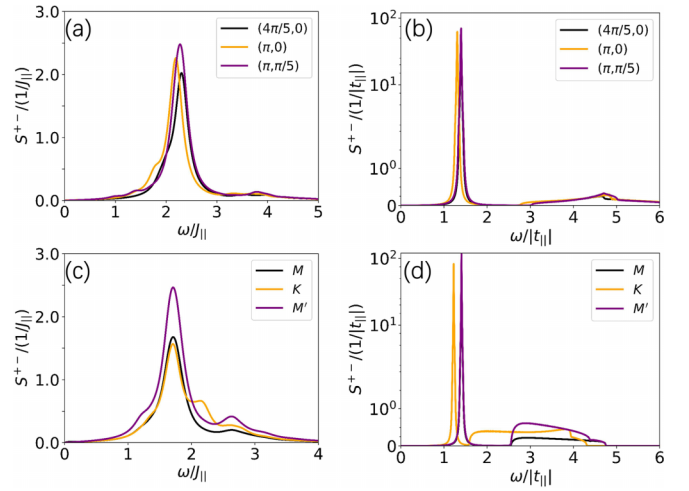


FIG. 7. (a) and (b) Dynamical structure factors for the square lattice at the two-dimensional limit from cluster perturbation theory (CPT) and random-phase-approximation (RPA) methods, respectively. (c) and (d) Dynamical structure factors for the honeycomb lattice at the two-dimensional limit from the CPT and RPA methods, respectively.

the two-dimensional Heisenberg model with $J_{\perp}/J_{\parallel} = 1$, the two-dimensional spinon Hubbard model with $t_{\perp}/t_{\parallel} = 1$ also has a significant continuum at the $(\pi, 0)$ point that is close to the magnon in energy. In the RPA analysis of the spinon Hubbard model, the minimum of the continuum at the $(\pi, 0)$ point comes from the two-spin excitations composed of the two lowest-energy spinons at $(\pm\pi/2, \pm\pi/2)$ [see Eq. (13)], whose momentum difference is exactly $(\pm\pi, 0)$ and $(0, \pm\pi)$. Since the two-spin continuum and the single-magnon excitation are closest in energy at the $(\pi, 0)$ point, the coupling between them is strongest at this point. As a result, it is most likely that one magnon will decay into two spinons, leading to the deconfinement of spinons. Additionally, the coupling between magnon and spinon creates a local minimum at the $(\pi, 0)$ point in the magnon dispersion. Equation (13) shows that the momentum position of the minimum of the spinon dispersion remains unchanged with variations in the interchain coupling, which explains why the local minimum of the magnon dispersion is fixed at the $(\pi, 0)$ point and does not change with the interchain couplings in both CPT and RPA results. Furthermore, the lowest-energy spinons at $(\pm\pi/2, \pm\pi/2)$ can not only produce the minimum of the two-spinon continuum at the $(\pi, 0)$ point but also the minimum at the (π, π) point [see Fig. 6(c)]. This observation is also consistent with the CPT result [see Fig. 2(f)].

For the honeycomb lattice, the spectra with the mean-field order parameter of $m = 0.25$ are presented in Figs. 6(d)–6(f). The same as the square lattice, the RPA analysis of the spinon Hubbard model for the honeycomb lattice also captures the key features of the spin-excitation spectra obtained from the CPT calculations of the Heisenberg model described above. Both the RPA and CPT results reveal that the magnon dispersion has a local minimum in the M - K direction, and the position of the minimum shifts with the change of the interchain couplings. In both cases where $t_{\perp}/t_{\parallel} = 1$ and $J_{\perp}/J_{\parallel} = 1$, this minimum is located at the K point. This local minimum

of the magnon dispersion also comes from the magnon-spinon coupling, as there is a minimum of the two-spinon continuum close to the magnon energy at the same momentum point. According to Eq. (14), the location of the minimum in the spinon dispersion changes with t_{\perp} , causing a corresponding shift in the minimum of the two-spinon continuum and consequently resulting in the change of the minimum of the magnon dispersion as well. At $t_{\perp}/t_{\parallel} = 1$, the minimum of the two-spinon continuum moves to the K point, resulting in a strong coupling between magnons and spinons and consequently the spinon deconfinement. This explains why both experimental observations and CPT calculations show the most significant continuum at the K point for $J_{\perp}/J_{\parallel} = 1$. Additionally, as shown in Fig. 6(f), we note that the dome-shaped structure of the continuum as well as the characteristics of its lower boundary are consistent with the results obtained from CPT calculations based on the Heisenberg model [Fig. 4(f)].

Therefore, according to the above discussion, the comparison between the CPT and RPA results (also refer to Fig. 7) further supports the spinon-deconfinement mechanism as the origin of the anomalous continuum observed in experiments in the AFM Néel states. Moreover, the agreement between the CPT and RPA results provides a more lucid explanation of the mechanism.

IV. SUMMARY

In this paper, we used the spin-CPT method to investigate the evolution of the spin-excitation spectrum of the mixed-dimensional Heisenberg model on square and honeycomb lattices by varying J_{\perp}/J_{\parallel} . We uncover detailed evolutions of the spectra of two-spinon continua and magnons with J_{\perp}/J_{\parallel} . At the two-dimensional limit with $J_{\perp}/J_{\parallel} = 1$, there remains a distinct high-energy continuum in the AFM Néel phases. Specifically, for the square lattice, the continuum is mainly concentrated at the $(\pi, 0)$ point, and for the honeycomb lattice, a dome-shaped continuum around the Γ' point is formed with its maximal intensity at the K point. Our results suggest

that the continuum at high energies in the two-dimensional limit results from the deconfinement of spinons. To further support this mechanism, we use the RPA method to obtain the spin-excitation spectra of the spinon Hubbard models in the AFM Néel phases. All the key features of the continua and magnon dispersions in the CPT result are successfully reproduced in the RPA calculations, where the continua arise from the particle-hole excitations corresponding to the two-spinon excitations. Thus, our results reveal that the continua at high energies of the AFM Néel phases originate from the mechanism of the spinon deconfinement.

ACKNOWLEDGMENTS

This paper was supported by the National Key Projects for Research and Development of China (Grant No. 2021YFA1400400) and National Natural Science Foundation of China (Grants No. 92165205 and No. 12074175).

APPENDIX: DETAILED COMPARISONS OF CPT AND RPA RESULTS AT SPECIFIC MOMENTA

In the main text, we present the spin-dynamical structure factors obtained from the CPT and RPA calculations along the paths consisting of high-symmetry lines in the BZ. Here, we provide the energy distributions of the dynamical structure factors at special momenta to facilitate a detailed comparison between the results obtained from the CPT and RPA calculations at the two-dimensional limit (with $J_{\perp}/J_{\parallel} = 1$ and $t_{\perp}/t_{\parallel} = 1$). In Figs. 7(a) and 7(b), we display the dynamical structure factors at three momenta for the square lattice from the CPT and RPA methods, respectively. It is evident that the non-Lorentzian tails at high energies in both cases are consistent, including their onset energies and the distributions. The dynamical structure factors for the honeycomb lattice from the CPT and RPA methods are presented in Figs. 7(c) and 7(d), respectively. Like the square lattice, the onset energies and distributions of the high-energy continua obtained from the CPT and RPA calculations also demonstrate good consistency.

-
- [1] L. Faddeev and L. Takhtajan, *Phys. Lett. A* **85**, 375 (1981).
 - [2] A. C. Walters, T. G. Perring, J.-S. Caux, A. T. Savici, G. D. Gu, C.-C. Lee, W. Ku, and I. A. Zaliznyak, *Nat. Phys.* **5**, 867 (2009).
 - [3] B. Lake, A. M. Tsvelik, S. Notbohm, D. A. Tennant, T. G. Perring, M. Reehuis, C. Sekar, G. Krabbes, and B. Büchner, *Nat. Phys.* **6**, 50 (2010).
 - [4] M. Mourigal, M. Enderle, A. Klöpperpieper, J.-S. Caux, A. Stunault, and H. M. Rønnow, *Nat. Phys.* **9**, 435 (2013).
 - [5] A. K. Bera, B. Lake, F. H. L. Essler, L. Vanderstraeten, C. Hubig, U. Schollwöck, A. T. M. N. Islam, A. Schneidewind, and D. L. Quintero-Castro, *Phys. Rev. B* **96**, 054423 (2017).
 - [6] L. S. Wu, S. E. Nikitin, Z. Wang, W. Zhu, C. D. Batista, A. M. Tsvelik, A. M. Samarakoon, D. A. Tennant, M. Brando, L. Vasylechko *et al.*, *Nat. Commun.* **10**, 698 (2019).
 - [7] L. J. P. Ament, M. van Veenendaal, T. P. Devereaux, J. P. Hill, and J. van den Brink, *Rev. Mod. Phys.* **83**, 705 (2011).
 - [8] J. Schlappa, K. Wohlfeld, K. Zhou, M. Mourigal, M. Haverkort, V. Strocov, L. Hozoi, C. Monney, S. Nishimoto, S. Singh *et al.*, *Nature (London)* **485**, 82 (2012).
 - [9] J. Schlappa, U. Kumar, K. Zhou, S. Singh, M. Mourigal, V. Strocov, A. Revcolevschi, L. Patthey, H. Rønnow, S. Johnston *et al.*, *Nat. Commun.* **9**, 5394 (2018).
 - [10] U. Kumar, A. Nag, J. Li, H. C. Robarts, A. C. Walters, M. García-Fernández, R. Saint-Martin, A. Revcolevschi, J. Schlappa, T. Schmitt *et al.*, *Phys. Rev. B* **106**, L060406 (2022).
 - [11] H. Bethe, *Z. Phys.* **71**, 205 (1931).
 - [12] J. des Cloizeaux and J. J. Pearson, *Phys. Rev.* **128**, 2131 (1962).
 - [13] T. Yamada, *Prog. Theor. Phys.* **41**, 880 (1969).
 - [14] X. G. Wen, *Phys. Rev. B* **44**, 2664 (1991).
 - [15] L. Balents, *Nature (London)* **464**, 199 (2010).
 - [16] T.-H. Han, J. S. Helton, S. Chu, D. G. Nocera, J. A. Rodriguez-Rivera, C. Broholm, and Y. S. Lee, *Nature (London)* **492**, 406 (2012).
 - [17] Y. Zhou, K. Kanoda, and T.-K. Ng, *Rev. Mod. Phys.* **89**, 025003 (2017).
 - [18] J. Wen, S.-L. Yu, S. Li, W. Yu, and J.-X. Li, *npj Quantum Mater.* **4**, 12 (2019).

- [19] C. Broholm, R. Cava, S. Kivelson, D. Nocera, M. Norman, and T. Senthil, *Science* **367**, eaay0668 (2020).
- [20] W. Zheng, J. O. Fjærestad, R. R. P. Singh, R. H. McKenzie, and R. Coldea, *Phys. Rev. Lett.* **96**, 057201 (2006).
- [21] N. B. Christensen, H. M. Rønnow, D. F. McMorrow, A. Harrison, T. G. Perring, M. Enderle, R. Coldea, L. P. Regnault, and G. Aeppli, *Proc. Natl. Acad. Sci. USA* **104**, 15264 (2007).
- [22] N. S. Headings, S. M. Hayden, R. Coldea, and T. G. Perring, *Phys. Rev. Lett.* **105**, 247001 (2010).
- [23] B. Dalla Piazza, M. Mourigal, N. B. Christensen, G. J. Nilsen, P. Tregenna-Piggott, T. G. Perring, M. Enderle, D. F. McMorrow, D. A. Ivanov, and H. M. Rønnow, *Nat. Phys.* **11**, 62 (2015).
- [24] H. Shao, Y. Q. Qin, S. Capponi, S. Chesi, Z. Y. Meng, and A. W. Sandvik, *Phys. Rev. X* **7**, 041072 (2017).
- [25] F. Ferrari and F. Becca, *Phys. Rev. B* **98**, 100405(R) (2018).
- [26] S.-L. Yu, W. Wang, Z.-Y. Dong, Z.-J. Yao, and J.-X. Li, *Phys. Rev. B* **98**, 134410 (2018).
- [27] A. Thomson and S. Sachdev, *Phys. Rev. X* **8**, 011012 (2018).
- [28] F. Ferrari and F. Becca, *Phys. Rev. X* **9**, 031026 (2019).
- [29] Z.-Y. Dong, W. Wang, Z.-L. Gu, S.-L. Yu, and J.-X. Li, *Phys. Rev. B* **102**, 224417 (2020).
- [30] F. Ferrari and F. Becca, *J. Phys.: Condens. Matter* **32**, 274003 (2020).
- [31] C. Zhang and T. Li, *Phys. Rev. B* **102**, 075108 (2020).
- [32] W. Wan, N. B. Christensen, A. W. Sandvik, P. Tregenna-Piggott, G. J. Nilsen, M. Mourigal, T. G. Perring, C. D. Frost, D. F. McMorrow, and H. M. Rønnow, *J. Phys.: Condens. Matter* **32**, 374007 (2020).
- [33] L. Testa, V. Šurija, K. Prša, P. Steffens, M. Boehm, P. Bourges, H. Berger, B. Normand, H. M. Rønnow, and I. Živković, *Phys. Rev. B* **103**, L020409 (2021).
- [34] Z.-Y. Dong, W. Wang, Z.-L. Gu, and J.-X. Li, *Phys. Rev. B* **104**, L180406 (2021).
- [35] L. Yang and A. E. Feiguin, *SciPost Phys.* **10**, 110 (2021).
- [36] L. Martinelli, D. Betto, K. Kummer, R. Arpaia, L. Braicovich, D. Di Castro, N. B. Brookes, M. Moretti Sala, and G. Ghiringhelli, *Phys. Rev. X* **12**, 021041 (2022).
- [37] C. Gu, S.-L. Yu, and J.-X. Li, *Phys. Rev. B* **105**, 174403 (2022).
- [38] G. Sala, M. B. Stone, B. K. Rai, A. F. May, P. Laurell, V. O. Garlea, N. P. Butch, M. D. Lumsden, G. Ehlers, G. Pokharel *et al.*, *Nat. Commun.* **12**, 171 (2021).
- [39] C. Wessler, B. Roessli, K. W. Krämer, B. Delley, O. Waldmann, L. Keller, D. Cheptikov, H. B. Braun, and M. Kenzelmann, *npj Quantum Mater.* **5**, 85 (2020).
- [40] I. Affeck, M. P. Gelfand, and R. R. P. Singh, *J. Phys. A: Math. Gen.* **27**, 7313 (1994).
- [41] D. J. Scalapino, Y. Imry, and P. Pincus, *Phys. Rev. B* **11**, 2042 (1975).
- [42] H. J. Schulz, *Phys. Rev. Lett.* **77**, 2790 (1996).
- [43] A. W. Sandvik, *Phys. Rev. Lett.* **83**, 3069 (1999).
- [44] V. Y. Irkhin and A. A. Katanin, *Phys. Rev. B* **61**, 6757 (2000).
- [45] Y. J. Kim and R. J. Birgeneau, *Phys. Rev. B* **62**, 6378 (2000).
- [46] L. Facheris, S. D. Nabi, A. Glezer Moshe, U. Nagel, T. Rööm, K. Yu. Povarov, J. R. Stewart, Z. Yan, and A. Zheludev, *Phys. Rev. Lett.* **130**, 256702 (2023).
- [47] W. J. Gannon, I. A. Zaliznyak, L. S. Wu, A. E. Feiguin, A. M. Tsvelik, F. Demmel, Y. Qiu, J. R. D. Copley, M. S. Kim, and M. C. Aronson, *Nat. Commun.* **10**, 1123 (2019).
- [48] B. Lake, D. A. Tennant, and S. E. Nagler, *Phys. Rev. Lett.* **85**, 832 (2000).
- [49] M. Kenzelmann, A. Zheludev, S. Raymond, E. Ressouche, T. Masuda, P. Böni, K. Kakurai, I. Tsukada, K. Uchinokura, and R. Coldea, *Phys. Rev. B* **64**, 054422 (2001).
- [50] B. Lake, D. A. Tennant, and S. E. Nagler, *Phys. Rev. B* **71**, 134412 (2005).
- [51] H. Zhang, Z. Zhao, D. Gautreau, M. Raczkowski, A. Saha, V. O. Garlea, H. Cao, T. Hong, H. O. Jeschke, S. D. Mahanti *et al.*, *Phys. Rev. Lett.* **125**, 037204 (2020).
- [52] C.-M. Ho, V. N. Muthukumar, M. Ogata, and P. W. Anderson, *Phys. Rev. Lett.* **86**, 1626 (2001).
- [53] O. F. Syljuåsen and P. A. Lee, *Phys. Rev. Lett.* **88**, 207207 (2002).
- [54] D. Sénéchal, D. Perez, and M. Pioro-Ladrière, *Phys. Rev. Lett.* **84**, 522 (2000).
- [55] M. G. Zacher, R. Eder, E. Arrigoni, and W. Hanke, *Phys. Rev. Lett.* **85**, 2585 (2000).
- [56] D. Sénéchal and A.-M. S. Tremblay, *Phys. Rev. Lett.* **92**, 126401 (2004).
- [57] S.-L. Yu, X. C. Xie, and J.-X. Li, *Phys. Rev. Lett.* **107**, 010401 (2011).
- [58] S.-L. Yu and J.-X. Li, *Phys. Rev. B* **85**, 144402 (2012).
- [59] T. Matsubara and H. Matsuda, *Prog. Theor. Phys.* **16**, 569 (1956).
- [60] W. Koller and N. Dupuis, *J. Phys.: Condens. Matter* **18**, 9525 (2006).
- [61] M. Knap, E. Arrigoni, and W. von der Linden, *Phys. Rev. B* **83**, 134507 (2011).
- [62] E. Dagotto, *Rev. Mod. Phys.* **66**, 763 (1994).
- [63] See Supplemental Material at <http://link.aps.org/supplemental/10.1103/PhysRevB.108.224418> for detailed information on the CPT calculation for the Heisenberg chain and the CPT results obtained from different cluster sizes and structures
- [64] H. B. Thacker, *Rev. Mod. Phys.* **53**, 253 (1981).
- [65] B. Lake, D. A. Tennant, J.-S. Caux, T. Barthel, U. Schollwöck, S. E. Nagler, and C. D. Frost, *Phys. Rev. Lett.* **111**, 137205 (2013).
- [66] F. Ferrari, A. Parola, S. Sorella, and F. Becca, *Phys. Rev. B* **97**, 235103 (2018).
- [67] J.-Q. Cheng, J. Li, Z. Xiong, H.-Q. Wu, A. W. Sandvik, and D.-X. Yao, *npj Quantum Mater.* **7**, 3 (2022).
- [68] K. Majumdar, *Phys. Rev. B* **82**, 144407 (2010).
- [69] T. C. Hsu, *Phys. Rev. B* **41**, 11379 (1990).
- [70] J. R. Schrieffer, X. G. Wen, and S. C. Zhang, *Phys. Rev. B* **39**, 11663 (1989).
- [71] N. M. R. Peres, M. A. N. Araújo, and D. Bozi, *Phys. Rev. B* **70**, 195122 (2004).
- [72] Q. Li, Y.-J. Wu, J. Yu, and J. He, *J. Phys.: Condens. Matter* **34**, 275602 (2022).